

# Localized Liquid-Phase Synthesis of Porous SnO<sub>2</sub> Nanotubes on MEMS Platform for Low-Power, High Performance Gas Sensors

Incheol Cho,<sup>†</sup> Kyungnam Kang,<sup>†</sup> Daejong Yang,<sup>‡</sup> Jeonghoon Yun,<sup>†</sup> and Inkyu Park<sup>\*,†</sup>

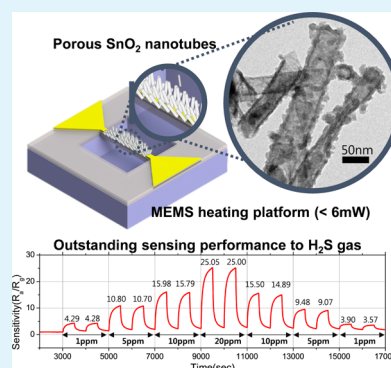
<sup>†</sup>Department of Mechanical Engineering, Korea Advanced Institute of Science and Technology (KAIST), 291 Daehak-ro, Yuseong-gu, Daejeon 305-701, South Korea

<sup>‡</sup>Department of Medical Engineering, California Institute of Technology, Pasadena, California 91125, United States

## Supporting Information

**ABSTRACT:** We have developed highly sensitive, low-power gas sensors through the novel integration method of porous SnO<sub>2</sub> nanotubes (NTs) on a micro-electro-mechanical-systems (MEMS) platform. As a template material, ZnO nanowires (NWs) were directly synthesized on beam-shaped, suspended microheaters through an in situ localized hydrothermal reaction induced by local thermal energy around the Joule-heated area. Also, the liquid-phase deposition process enabled the formation of a porous SnO<sub>2</sub> thin film on the surface of ZnO NWs and simultaneous etching of the ZnO core, eventually to generate porous SnO<sub>2</sub> NTs. Because of the localized synthesis of SnO<sub>2</sub> NTs on the suspended microheater, very low power for the gas sensor operation (<6 mW) has been realized. Moreover, the sensing performance (e.g., sensitivity and response time) of synthesized SnO<sub>2</sub> NTs was dramatically enhanced compared to that of ZnO NWs. In addition, the sensing performance was further improved by forming SnO<sub>2</sub>-ZnO hybrid nanostructures due to the heterojunction effect.

**KEYWORDS:** metal oxide, gas sensor, MEMS, tin oxide (SnO<sub>2</sub>), nanowire, nanotube, liquid-phase deposition



## INTRODUCTION

Nowadays, there is a growing demand for mobile and personalized environmental monitoring. For example, personal mobile gas sensors are used to monitor the indoor air quality or detect natural disasters, as well as for healthcare applications such as breath-based early diagnosis of diseases. Also, mobile gas sensors are used in the industry to increase the yield of products or to ensure the safety of workers. Among various types of gas sensors, semiconductor metal oxide (SMO) gas sensors are suitable for mobile applications due to their small size, low cost, and high sensitivity.<sup>1</sup> However, they usually need high operation temperatures ranging from 200 to 400 °C thus requiring high electrical power for heating. To reduce the operating power, researchers have tried to combine microheating platforms and sensing nanomaterials. Most widely used approaches are based on drop casting or printing (e.g., inkjet printing, screen printing, etc.) of nanomaterials that were presynthesized through chemical vapor deposition (CVD), physical vapor deposition, and sol-gel methods.<sup>2-4</sup> Although these methods are simple, they require additional steps to form a stable liquid solution of nanomaterials and suffer from limited downscaling of the integration area due to poor patterning resolution. For example, Zhou et al. developed ultralow-power microheaters that require only 2 mW of power at 300 °C for SMO gas sensors.<sup>5</sup> They developed a beam-shaped suspended structure to isolate the small heating spot. However, previously mentioned deposition methods did not allow fine integration of sensing nanomaterials on small selected areas, except for a thin film deposited with a shadow mask. Meanwhile, Long et al. and

Xu et al. introduced a direct synthesis method of porous SnO<sub>2</sub> films on microheating platforms using an explosive evaporation method and a polystyrene bead-templated method, respectively.<sup>6,7</sup> Although nanoscale sensing materials were well formed on microheaters, there were limitations in applying them on a suspended microstructure<sup>6</sup> or on a very small area (e.g., diameter < 10 μm)<sup>7</sup> due to their fabrication mechanisms.

In our previous study, we reported a localized hydrothermal synthesis method for ZnO nanowires, CuO nanospikes, and TiO<sub>2</sub> nanotubes (NTs).<sup>8-13</sup> When an electrical voltage is applied across the prefabricated microheaters submerged in the liquid precursor, the temperature rise around the localized Joule-heated region induces a hydrothermal reaction of the precursor chemicals. Also, as convective heat transfer followed by convective mass transfer of the precursor is generated, fresh precursors are continuously supplied to the reaction area where the endothermal reaction continues a selective synthesis of nanomaterials. This method has enabled a direct integration of one-dimensional (1-D) nanomaterials onto the desired spot along microheaters. However, microheaters were bound on the substrate (i.e., not suspended from the substrate) and thus required high electrical power for heating due to significant conductive heat dissipation to the substrate. Furthermore, this method could not be applied to 1-D SnO<sub>2</sub> nanomaterials, which are known to possess outstanding gas sensing performances

Received: April 6, 2017

Accepted: July 17, 2017

Published: July 17, 2017

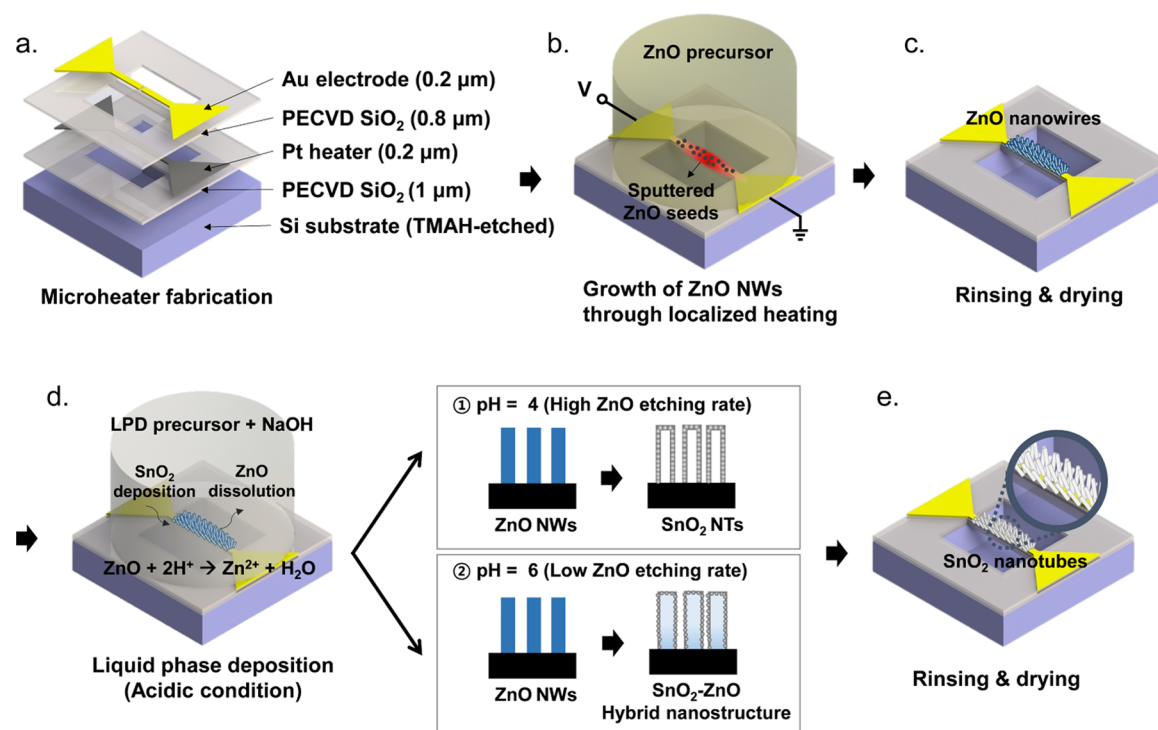


**Figure 1.** Scheme of localized synthesis of ZnO NW and SnO<sub>2</sub> NT on the MEMS microheater: (a) Illustration of whole layers of the microheater; (b, c) localized hydrothermal synthesis of ZnO NWs on the Joule-heated area; (d, e) LPD for substituting locally synthesized ZnO NWs to SnO<sub>2</sub> NTs. The deposition of the SnO<sub>2</sub> thin film and dissolution of ZnO NWs occur simultaneously. The etching rate of ZnO is determined by the pH of the LPD precursor. A small amount of 1 M NaOH was added to adjust the pH to 4 and 6. Each condition generates SnO<sub>2</sub> NTs and SnO<sub>2</sub>-ZnO hybrid nanostructures.

and excellent stability,<sup>14</sup> due to the lack of their hydrothermal synthesis methods in liquid environment under atmospheric pressure conditions.

This article introduces a novel integration method of 1-D SnO<sub>2</sub> nanomaterials on suspended micro-electro-mechanical-systems (MEMS) microheaters to achieve high sensitivity, great stability, outstanding response speed, and low-power consumption for the detection of toxic gases. The suspended structure of MEMS microheaters thermally isolates the heating spot from the Si substrate. Through the optimal design of the suspended microheater, heat loss to the substrate has been dramatically reduced, facilitating very low heating power for the gas detection (<6 mW). Also, we directly synthesized porous SnO<sub>2</sub> NTs on suspended microheaters in a low-cost, fast, and low-temperature liquid-phase process. First, ZnO NWs were synthesized on MEMS microheaters through a localized hydrothermal reaction. To enhance the gas sensing performances (i.e., sensitivity, response speed, and stability), we substituted presynthesized ZnO NWs with SnO<sub>2</sub> NTs via the liquid-phase deposition (LPD) process along ZnO NW templates. Because of the acidic condition (i.e., low pH) of the LPD solution, ZnO NWs were etched out simultaneously. In this step, we could control the amount of ZnO remaining in the SnO<sub>2</sub> NTs by controlling the condition of LPD for the modulation of sensing characteristics. This method allows facile integration of high performance 1-D sensing nanomaterials on selected and suspended microscale spots, which is difficult to achieve by other conventional methods. Furthermore, we demonstrated that this method can be applied to complex-shaped microheaters, such as a suspended structure, which was not previously realized, resulting in application for low-power gas sensors.

## ■ MATERIALS AND METHODS

**Design and Fabrication of Microheaters.** To minimize the operating power of the gas sensor, the MEMS microheater was designed with optimized geometry. To minimize the amount of heat dissipation to the silicon substrate and the size of the heating area, a beam-shaped heater structure was selected. The width and length of the beam can be optimized through the heat-transfer analysis and constraint of fabrication capability. The heat dissipation from the microheater is caused by conductive, convective, and radiative heat-transfer modes. Considering the microscale size of the heating area, the operating temperature range (25–300 °C), and the magnitude of the various heat-transfer coefficients, convective and radiative heat losses are negligibly small compared to the conductive heat loss (see the section “Design of Microheaters” in the Supporting Information for more detail). Therefore, only the conductive heat transfer to the substrate through the heater beam and air was considered, whereas the convective and radiative heat dissipations were neglected. As a consequence, the optimal geometry of the beam for minimizing the heat loss was 3 μm in width and 110 μm in length (see Figure S1 in the Supporting Information).

Figure 1a shows the structure of the MEMS microheater, including a structural layer, an insulation layer, and metal electrodes. The microheater was fabricated using conventional MEMS processes. (1) First, a SiO<sub>2</sub> layer was deposited with a thickness of 1 μm by the plasma-enhanced chemical vapor deposition (PECVD) process on the silicon wafer. (2) Then, polymethylglutarimide (PMGI) and photoresist (AZ5214; MicroChemicals, Germany) were spin-coated to lift off the Pt heater and the shape of the microheater was patterned with UV photolithography. (3) Subsequently, Ti/Pt (thickness of 10/200 nm, respectively) was deposited by electron beam evaporation and the PMGI layer and AZ5214 layer were removed with a developer (AZ300 MIF; AZ Electronic Materials) and acetone. (4) An 800 nm thick SiO<sub>2</sub> layer was deposited by the PECVD process for electrical insulation between the heater and sensing electrodes. (5) Cr/Au (10/200 nm thickness each) sensing electrodes were patterned by the same

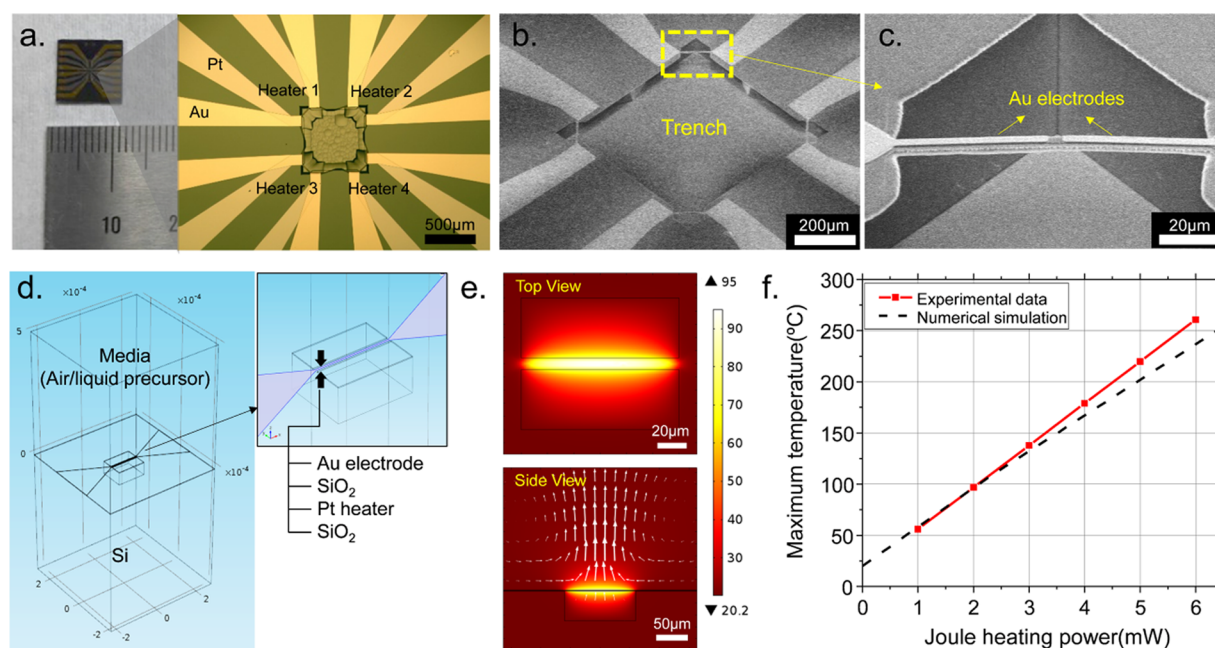


**Figure 2.** (a) Photo of the fabricated sensor chip; (b, c) SEM images of fabricated microheaters:  $2 \times 2$  arrays of the microheater on a single chip (b) and a suspended and beam-shaped microheater (c); (d) geometries and materials of the microheater for numerical simulation; (e) results of the numerical simulation for temperature distribution around the microheater in aqueous ZnO precursor in top view (top) and side view (bottom). Free convection of the aqueous precursor was generated due to local heating; (f) estimated relationship between the maximum temperature and heating power of the microheater in room-temperature air environment through experimental data (resistive temperature detection) and numerically calculated data.

method, as that in step (3). (6) The  $\text{SiO}_2$  insulating layer covering the pad of the Pt heater was removed by photolithography and buffered oxide etchant etching. (7) Before the Si bulk etching, an etching window was patterned by UV photolithography (AZ9260 photoresist; AZ Electronic Materials) and reactive ion etching to expose the Si substrate. (8) Samples were annealed in a nitrogen atmosphere at  $350^\circ\text{C}$  for 1 h to relax residual stresses of the PECVD  $\text{SiO}_2$  layer. (9) Finally, Si bulk etching was carried out using tetramethylammonium hydroxide wet etching to obtain the suspended microheater beam.

Numerical simulations and resistive temperature detection (RTD) were conducted to verify the heating performance of the fabricated microheater. The temperature distribution of the Joule-heated region in liquid precursor and mass convection of the precursor were estimated with Joule heating, heat conduction, and convective flow models in COMSOL Multiphysics to verify the area where the hydrothermal reaction occurs. Also, the relationship between temperature and heating power in atmosphere was measured via the resistive temperature detection (RTD) method to estimate the operating power of the gas sensor (experimental detail is explained in the Supporting Information).

**Synthesis of ZnO Nanowires and  $\text{SnO}_2$  Nanotubes.** Overall processes to synthesize ZnO NWs and  $\text{SnO}_2$  NTs are illustrated in Figure 1b–e. As seeds to grow ZnO NWs, ZnO nanoparticles were deposited by sputtering (100 W, 3 min) on fabricated MEMS microheaters. The ZnO precursor was prepared by dissolving 25 mM zinc nitrate hydrate, 25 mM hexamethylenetetramine, and 6 mM polyethyleneimine in deionized (DI) water (all chemicals were purchased from Sigma-Aldrich).<sup>15</sup> A PDMS well was attached to the sensor chip and filled with a few  $\mu\text{L}$  of ZnO precursor solution to submerge the fabricated microheater within the precursor solution. The voltage was applied to the microheater using tungsten probes and a source meter. When the microheater was heated with a power higher than 45 mW (voltage of 1.5 V and current of 30 mA), the precursor solution was boiled and bubbles were formed around the microheater. Therefore, the power was maintained at 45 mW, which is supposed to induce a local temperature of  $90\text{--}100^\circ\text{C}$  around the microheater. The synthesis was carried out for 15 min (total energy = 40.5 J). To avoid

the damage of the suspended microheater during the drying process, ethanol with low surface tension ( $22.1\text{ mN/m}$  at  $20^\circ\text{C}$ ) was utilized in the final rinsing and drying step.

After washing and drying, synthesized ZnO NWs were substituted to  $\text{SnO}_2$  NTs by filling the LPD precursor solution in the PDMS well attached to the sensor chip. The LPD precursor was prepared by dissolving 3.75 mM  $\text{SnF}_2$ , 15 mM of HF, 7.5 mM  $\text{H}_2\text{O}_2$ , and 37.5 mM  $\text{H}_3\text{BO}_3$  in DI water.<sup>16,17</sup> The initial pH of the LPD precursor solution was  $\sim 2$ . To control the amount of residual ZnO that exists on the inner surface of the  $\text{SnO}_2$  NT, pH of the LPD precursor solution was modulated by adding 1 M NaOH solution (controlled pH = 4 and 6). The condition (pH = 4) for a relatively high etching rate of ZnO was expected to form  $\text{SnO}_2$  NTs, whereas the condition (pH = 6) for a slower etching rate of ZnO was expected to form a hybrid nanostructure (i.e.,  $\text{SnO}_2$  NTs + ZnO residue). The processing time was fixed as 15 min for both pH conditions. After completion of the whole processes, samples were rinsed and dried with ethanol, as before. The detailed mechanism of LPD is explained in the section “Mechanism of Liquid-Phase Deposition of  $\text{SnO}_2$ ” in the Supporting Information.

**Measurement of Gas Concentration.** We selected  $\text{H}_2\text{S}$  gas as a target gas that is generated in rotten foods, natural gas, and oil refineries. High-concentration  $\text{H}_2\text{S}$  gas causes serious health problems, and its 8 h permissible exposure limit is 10 ppm. The  $\text{H}_2\text{S}$  gas sensing performance of the fabricated sensors was demonstrated by measuring their sensitivity to  $\text{H}_2\text{S}$  gas under various operating powers (3, 4, 5, and 6 mW). One to 20 ppm of  $\text{H}_2\text{S}$  gas was supplied into the chamber by balancing the flow rates of air and  $\text{H}_2\text{S}$  gas, and the total flow rate was 500 sccm. Electrical power for the microheater was provided using a direct current power supply (E3642A; Agilent), and the resistances of the three sensing materials (ZnO NW,  $\text{SnO}_2$  NT, and ZnO– $\text{SnO}_2$  hybrid nanostructure) were simultaneously measured by a source meter (SMU 2400; Keithley).

## RESULTS AND DISCUSSION

Figure 2a is an optical image of the fabricated sensor chip. The entire chip has a size of  $1 \times 1\text{ cm}^2$ . Figure 2b,c shows SEM

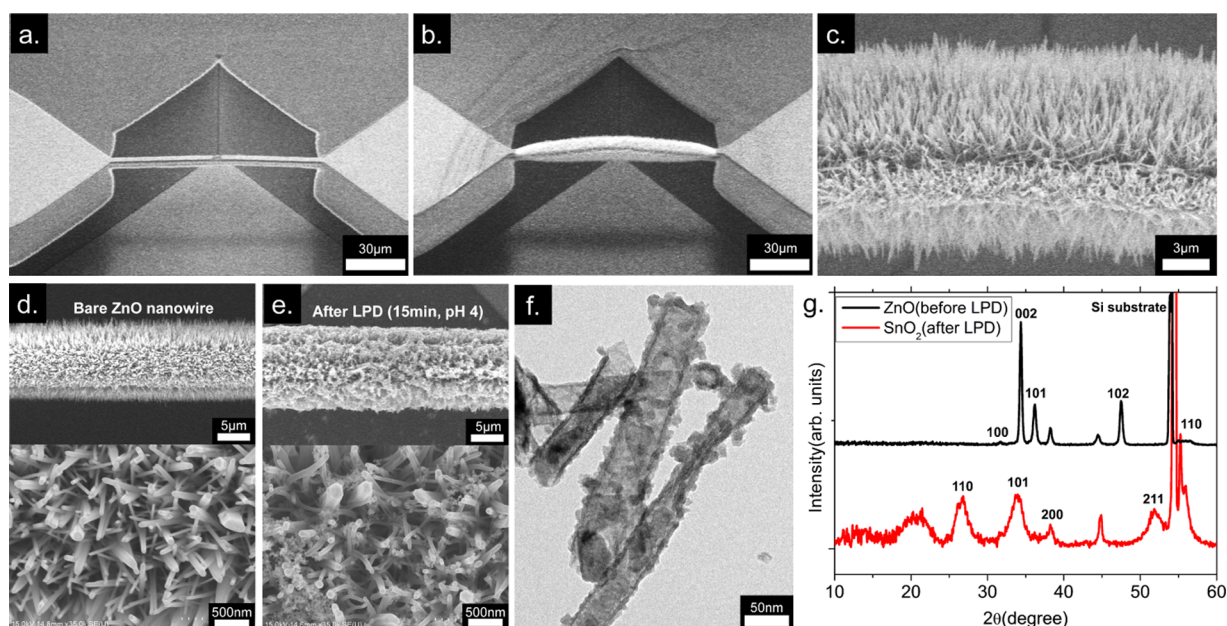


**Figure 3.** SEM images of (a) a microheater before synthesizing ZnO NWs and (b, c) after synthesizing ZnO NWs by the localized hydrothermal reaction; SEM images of locally synthesized (d) ZnO NWs before LPD and (e) SnO<sub>2</sub> NTs after LPD (pH = 4) for 15 min; (f) a TEM image of SnO<sub>2</sub> NTs synthesized by LPD at pH = 4; (g) XRD patterns of ZnO NWs and SnO<sub>2</sub> NTs synthesized at pH 4.

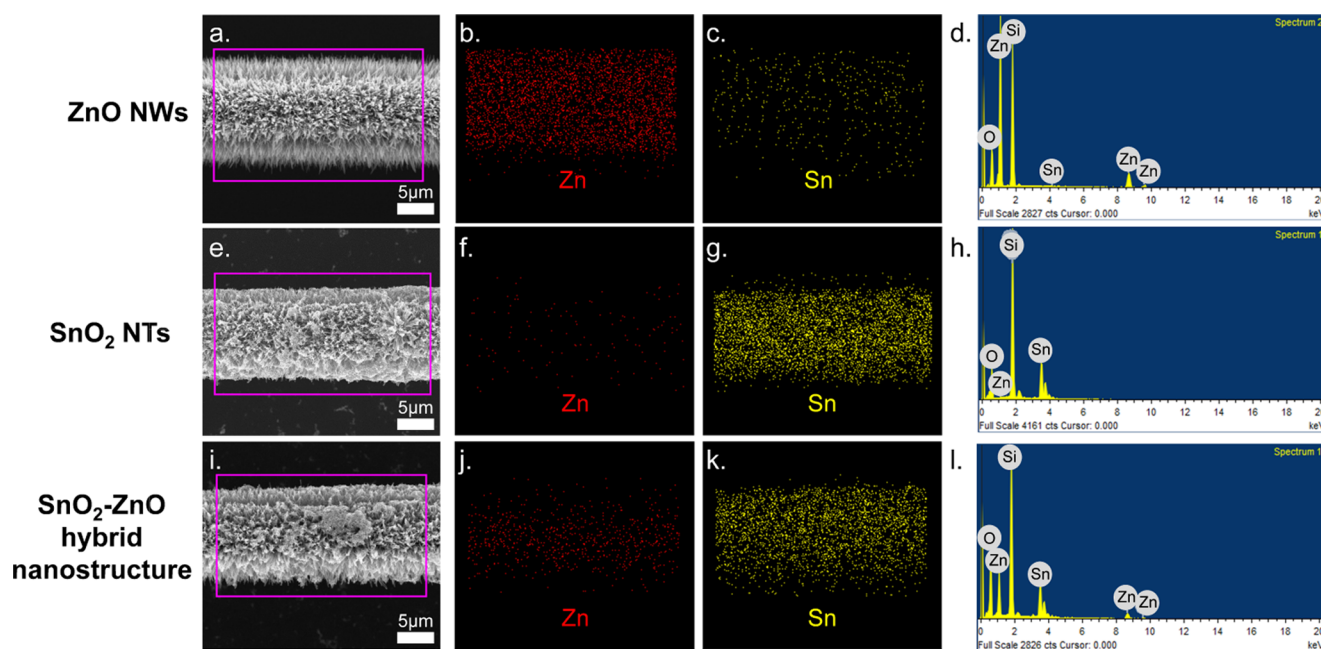


**Figure 4.** SEM-EDS analysis of locally synthesized nanostructures on MEMS microheater: (a) scanning area, (b, c) elemental mapping for Zn and Sn, (d) EDS spectra of ZnO NWs. (e–h), (i–l) Results in the case of SnO<sub>2</sub> NTs (LPD at pHs = 4 and 6, respectively) in the same order.

images of a  $2 \times 2$  array of microheaters on a single sensor chip and a suspended structure of a microheater. In the center of the sensor chip, a  $600 \mu\text{m}$ -sized trench is located for the easy penetration of the aqueous ZnO precursor beneath the microheater.

Figure 2d shows the three-dimensional model, including whole layers of a microheater and surrounding media (air or precursor solution) for numerical simulation of heat and mass transfer. As shown in Figure 2e, the maximum temperature reached about  $95^\circ\text{C}$  and the temperature gradually decreased toward the outside of the beam. Also, it is expected that molecules and ions used for the synthesis of ZnO NWs will be

continuously supplied to the microheater by free convection of the precursor solution by local heating of the microheater.

We measured the heating power of the microheater in atmospheric air conditions using the RTD method. The graph in Figure 2f shows the relationship between the maximum temperature on the microheater and the heating power. By carrying out several compensations explained in the Supporting Information (“Temperature–Power Relationship” section), the following relation was obtained.

$$\text{max temperature } (^\circ\text{C}) = 40.9 \times \text{power (mW)} + 15.2 \quad (1)$$

The power required to reach 300 °C, from the equation, is about 6.9 mW. Also, RTD data are close to the data derived from the numerical simulation (RMS error = 14.9 °C in the 1–6 mW range).

As shown in Figure 3a,b, ZnO NWs were locally synthesized on the beam-shaped suspended microheater. Similar to the temperature distribution along the microheater (Figure 1e), ZnO NWs were the longest at the center of the beam and gradually became shorter toward the anchor of the beam. The average (standard deviation) of diameters and lengths of ZnO NWs synthesized near the center of the beam were 67.7 nm ( $\pm 27$  nm) and 1.6  $\mu\text{m}$  ( $\pm 0.4$   $\mu\text{m}$ ), respectively (Figure 3c). Here, ZnO NWs form a complex network through numerous junctions between NWs. Figure 3d shows ZnO NWs before LPD and Figure 3e,f shows SnO<sub>2</sub> NTs after 15 min of LPD at pH = 4. Core ZnO NWs were etched out due to acidic condition of the LPD precursor. Therefore, translucent, porous, and granular tubelike structures were well formed and can be observed in the transmission electron microscopy (TEM) image of a SnO<sub>2</sub> NT synthesized at pH = 4 (Figure 3f). Figure 3g shows the X-ray diffraction (XRD) patterns of synthesized ZnO NWs and SnO<sub>2</sub> NTs. After LPD, the diffraction peaks from ZnO remarkably decreased, whereas those of rutile SnO<sub>2</sub> were clearly observed. This result also indicates that the surface of the ZnO NWs was well coated with crystallized SnO<sub>2</sub> and ZnO was effectively removed.

Figure 4 shows the SEM-energy dispersive spectroscopy (EDS) analysis of locally synthesized ZnO NWs and chemically converted SnO<sub>2</sub> NTs under different pH conditions on a microheater. Figure 4a–d shows the presence of Zn and Sn in the ZnO NWs through EDS element mapping. Zn (red dots) is much denser than Sn (yellow dots), which is represented quantitatively in Table 1 (atomic ratio: Zn = 25.23% and Sn =

**Table 1. Element Composition of ZnO NWs, SnO<sub>2</sub> NTs, and SnO<sub>2</sub>–ZnO Hybrid Nanostructures Obtained by EDS Analysis**

element	pristine ZnO nanowires		after LPD (15 min, pH = 4) SnO <sub>2</sub> nanotubes		after LPD (15 min, pH = 6) SnO <sub>2</sub> –ZnO hybrid nanostructures	
	wt %	atom %	wt %	atom %	wt %	atom %
O K	18.03	37.25	28.61	54.22	31.83	58.62
Si K	31.80	37.43	33.37	36.02	26.32	27.61
Zn L	49.89	25.23	0.21	0.10	16.71	7.53
Sn L	0.29	0.08	37.81	9.66	25.14	6.24

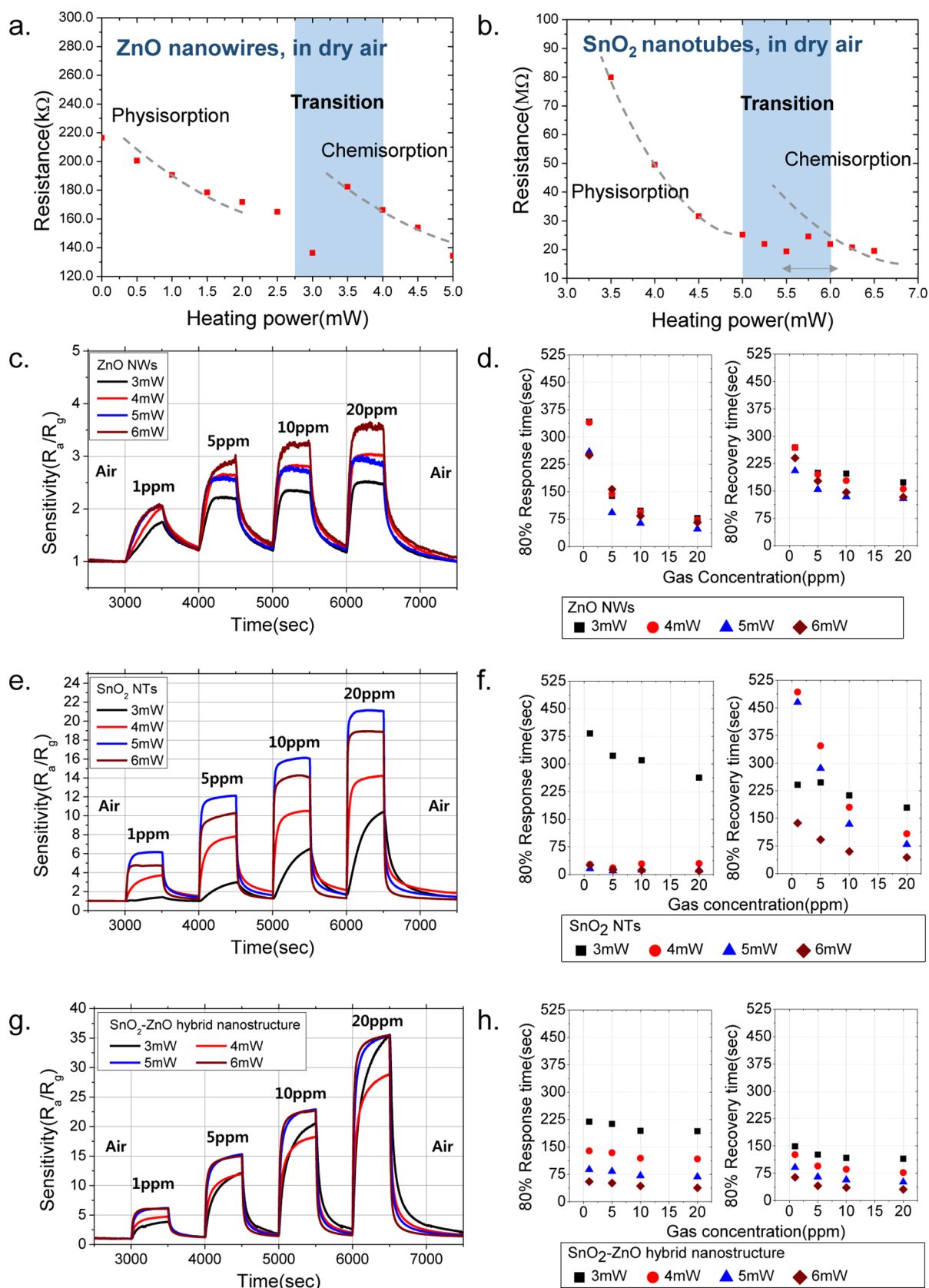
0.08%; here, the presence of Sn is ignorable due to measurement noise). Figure 4e–h shows the presence of Zn and Sn in SnO<sub>2</sub> NTs synthesized at pH = 4. As compared with ZnO NWs, Zn (red dots) is almost negligible, whereas Sn (yellow dots) is dramatically increased (atomic ratio: Zn = 0.1% and Sn = 9.66%, see Table 1; here, the presence of Zn is ignorable due to measurement noise). This is because ZnO was quickly etched while the SnO<sub>2</sub> layer was formed on the surface of the ZnO NW template (15 min) at pH = 4. On the other hand, Figure 4i–l shows similar presence of both Zn and Sn on the hybrid nanostructure synthesized at pH = 6. As expected, the amount of residual Zn (atomic ratio: Zn = 7.53% and Sn = 6.24%) was larger in this structure than that of the SnO<sub>2</sub> NTs synthesized at pH = 4. As a conclusion, it is possible to control the amount of ZnO remaining in the NTs by controlling the etching rate of ZnO at different pHs of the LPD solution. TEM

images of ZnO NWs, SnO<sub>2</sub> NTs, and SnO<sub>2</sub>–ZnO hybrid nanostructure are provided in Figure S4 in the Supporting Information.

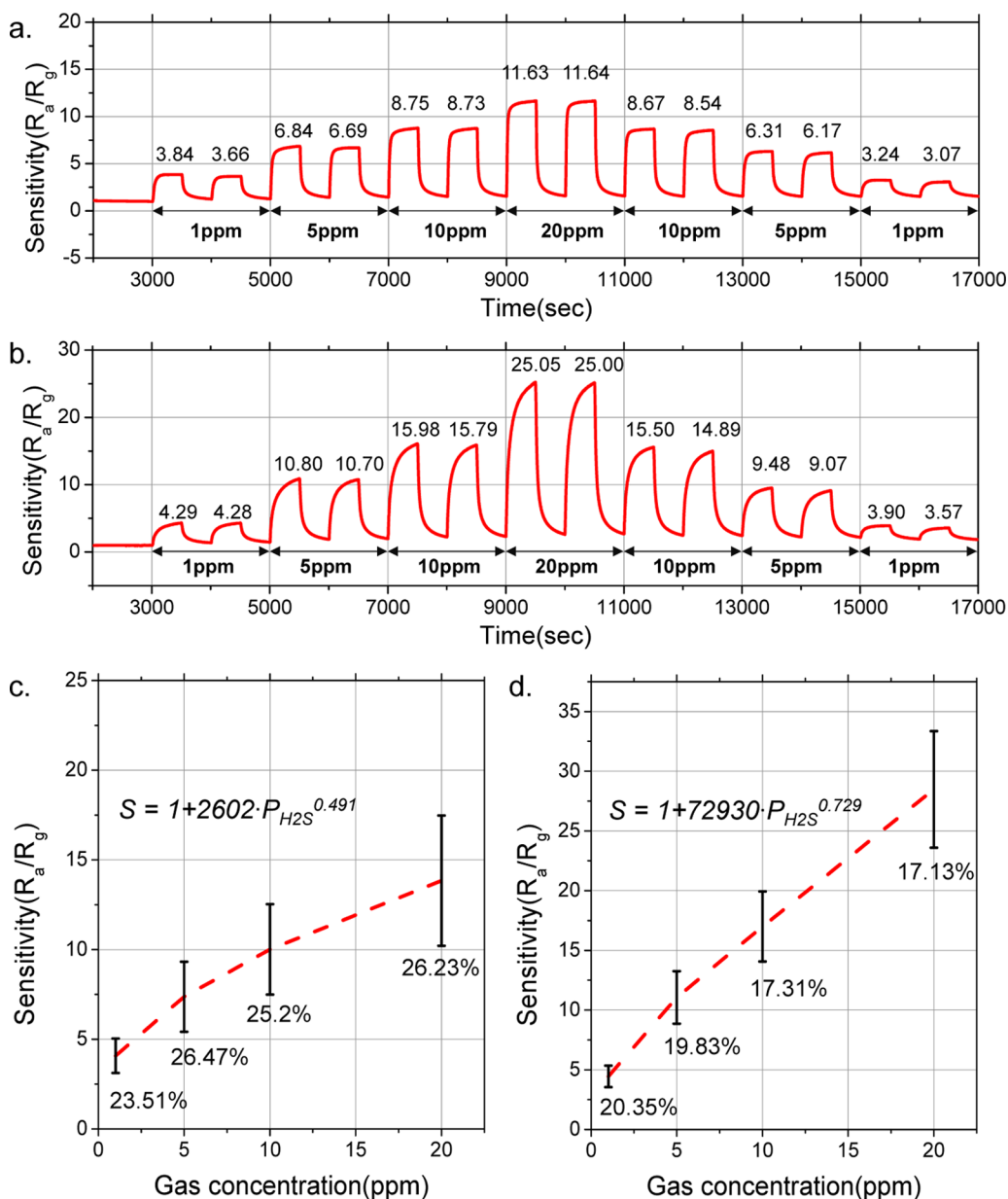
The adsorption state of oxygen molecules on the surface of the metal oxide depends on the temperature. The physisorption of O<sub>2</sub><sup>-</sup> and O<sup>-</sup> species with high adsorption–desorption rates dominates in the low-temperature range, whereas chemisorption of O<sup>2-</sup> with the low adsorption–desorption rate dominates in the high-temperature range.<sup>18</sup> In the physisorption region, the amount of adsorbed oxygen molecules is large, resulting in the high sensitivity. However, the adsorption of OH<sup>-</sup> dissociated from the water molecule is also active, and thus the sensor signal is greatly influenced by the humidity. On the other hand, in the chemisorption region, the OH<sup>-</sup> group is desorbed and the influence of moisture is reduced while the amount of O<sup>-</sup> adsorbed on the surface is reduced, resulting in the low sensitivity. Therefore, it is desirable to select an operating temperature in the transition region located between these two adsorption regimes. To select the proper operating power of the microheater on the basis of this theoretical background, the change of the sensing resistance according to the heating power ( $\propto$  heating temperature) was measured. Semiconductor materials generally exhibit decreasing electrical resistance at higher temperatures by the generation of electron–hole pairs induced by the thermal excitation. In the case of the metal oxide, as the temperature increases, a fluctuation of electrical resistance occurs in the declining tendency due to the changes of surface coverage of oxygen.<sup>19</sup>

Figure 6a,b shows the resistance change of ZnO NWs and SnO<sub>2</sub> NTs by varying the heating power of the microheater. Measurements were carried out in dry air (<5% RH) after the resistance of the heated sensing material was sufficiently stabilized. In the case of ZnO NWs, the resistance decreases until 3 mW ( $\sim 138$  °C), slightly rises in 3–3.5 mW ( $\sim 138$ – $158$  °C), and decreases again above 4 mW ( $\sim 179$  °C). It indicates that the physisorption is dominant in the low power range (<3 mW, 138 °C), whereas the chemisorption is dominant in the high power range (> 4 mW, 179 °C). Because the operating power of the SMO gas sensor is determined in the transition region between physisorption and chemisorption, as described above, the operating power of the ZnO NW can be chosen in the range between 3 and 4 mW. Similarly, Figure 5b shows the resistance change of SnO<sub>2</sub> NTs at different heating powers of the microheater. The resistance decreases until 4.5 mW ( $\sim 199$  °C), stagnates at 5–6 mW ( $\sim 220$ – $261$  °C), decreases again above 6.5 mW ( $\sim 281$  °C). Thus, the operating power of SnO<sub>2</sub> NTs can be determined in the range of 4.5–6 mW ( $\sim 199$ – $260$  °C). In general, it has been reported that the transition of O<sup>-</sup>/O<sub>2</sub><sup>-</sup> to O<sup>2-</sup> on the surface of SnO<sub>2</sub> takes place in the range of 190–300 °C,<sup>18</sup> which is similar to the temperature range determined from the experimental results. Therefore, the gas sensing tests for the ZnO NW and SnO<sub>2</sub> NT sensors were carried out in the range of 3–6 mW.

Sensitivity was defined as  $R_a/R_g$  ( $R_a$  = sensor resistance in ambient air,  $R_g$  = sensor resistance exposed to H<sub>2</sub>S gas). Because ZnO NWs and SnO<sub>2</sub> NTs are both n-type semiconductors, their resistances decrease when exposed to H<sub>2</sub>S (reducing gas). Figure 5c shows the dynamic response of the ZnO NW sensor locally synthesized on a microheater. The highest sensitivity was obtained when the ZnO NW was heated at 6 mW ( $R_a/R_g = 2.06$  at 1 ppm;  $R_a/R_g = 2.98$  at 5 ppm;  $R_a/R_g = 3.26$ ; and  $R_a/R_g = 3.60$  at 20 ppm). Figure 5d shows the 80% response and recovery times of ZnO NWs. The response and



**Figure 5.** Relationship of sensor resistance and heating power of (a) ZnO NWs and (b) SnO<sub>2</sub> NTs. Dashed lines represent physisorption and chemisorption regimes; H<sub>2</sub>S sensing results of fabricated sensor devices: (c, e, g) dynamic responses of bare ZnO NWs, SnO<sub>2</sub> NTs (synthesized at pH = 4), and SnO<sub>2</sub> NTs–ZnO hybrid nanostructures (synthesized at pH = 6), respectively, for different heating powers; (d, f, h) 80% response time and recovery time for each material and gas concentration (1, 5, 10, and 20 ppm).



**Figure 6.** Repeatability test for H<sub>2</sub>S sensing of (a) SnO<sub>2</sub> NTs and (b) SnO<sub>2</sub> NTs–ZnO hybrid nanostructures; sample-to-sample variation and calibration graph (dashed line) of (c) SnO<sub>2</sub> NTs and (d) SnO<sub>2</sub>–ZnO hybrid nanostructures with respect to the H<sub>2</sub>S concentrations.

recovery times were the shortest at 5 mW ( $t_{\text{rec}} = 205$  s/ $t_{\text{res}} = 93$  s at 1 ppm,  $t_{\text{rec}} = 154$  s/ $t_{\text{res}} = 64$  s at 5 ppm,  $t_{\text{rec}} = 134$  s/ $t_{\text{res}} = 48$  s at 10 ppm, and  $t_{\text{rec}} = 129$  s/ $t_{\text{res}} = 259$  s at 20 ppm). From these results, the ZnO NW sensor shows slightly long response and recovery times. Figure 5e shows the dynamic response of a SnO<sub>2</sub> NT sensor synthesized at pH = 4 on a microheater. SnO<sub>2</sub> NTs show the highest sensitivity at 5 mW heating power ( $R_a/R_g = 6.16$  at 1 ppm,  $R_a/R_g = 12.12$  at 5 ppm,  $R_a/R_g = 16.1$  at 10 ppm, and  $R_a/R_g = 21.07$  at 20 ppm). The sensitivity of SnO<sub>2</sub> NTs was 1.3 times (5 ppm, 3 mW) to 7.4 times (20 ppm, 5 mW) higher than that of ZnO NWs with the same power at all gas concentration ranges. Figure 5f summarizes the 80% response and recovery times of SnO<sub>2</sub> NTs. In all power ranges except at 3 mW, SnO<sub>2</sub> NTs showed very short response times (<30 s). The recovery time was in the range of 79–465 s, which showed faster recovery than ZnO NWs except for low concentrations (1 and 5 ppm). Figure 5g shows the dynamic

response of a SnO<sub>2</sub>–ZnO hybrid nanostructure synthesized at pH = 6 on the microheater. The highest sensitivity was obtained at 6 mW ( $R_a/R_g = 6.07$  at 1 ppm,  $R_a/R_g = 15.0$  at 5 ppm,  $R_a/R_g = 27.69$  at 10 ppm, and  $R_a/R_g = 35.31$  at 20 ppm). The sensitivity of SnO<sub>2</sub>–ZnO hybrid nanomaterials was higher than that of the SnO<sub>2</sub> NTs in all concentration ranges. However, as shown in Figure 5h, the 80% response time (36–55 s) of SnO<sub>2</sub>–ZnO hybrid nanostructure heated at a power over 4 mW was longer than that of SnO<sub>2</sub> NTs. The reason for the improved sensing performance of SnO<sub>2</sub> NTs and SnO<sub>2</sub>–ZnO hybrid nanostructures can be explained by the following two principles: The first is the effect of increased surface area. The NTs formed via the LPD process are expected to be air-permeable due to the porous and granular shell layer. Therefore, gas molecules can be in contact with the inner surface of the NTs, and thus the surface area-to-volume ratio can be remarkably increased compared to that of the NWs.

Second is the effect of the heterojunction. Numerous n–n junctions of SnO<sub>2</sub> and ZnO are formed due to the remaining ZnO on the inner surface of the SnO<sub>2</sub> NTs. The difference of work function between these two materials ( $\Phi_{\text{SnO}_2} = 4.9$  eV and  $\Phi_{\text{ZnO}} = 5.2$  eV) forms an additional carrier depletion layer. Therefore, it may cause a larger resistance change by reducing gas, such as H<sub>2</sub>S. Such a heterojunction effect improving the gas sensing performance has been experimentally demonstrated by various previous studies.<sup>20–28</sup> It is expected that the optimum pH condition of the LPD solution to maximize the sensing performances (i.e., the sensitivity and response time) can be found through further investigation.

Repeatability and sample-to-sample variation were verified to confirm the reliability of the fabricated sensor device. Repeatability tests were carried out by using two sensors with SnO<sub>2</sub> NTs and SnO<sub>2</sub>–ZnO hybrid nanostructures, respectively, with the same heating power (5 mW). The concentration of H<sub>2</sub>S gas was increased from 1 to 20 ppm. To investigate the existence of irreversible degradation of sensitivity after exposure to highly concentrated gas, the concentration of gas was decreased in a reverse sequence (20 to 1 ppm). Figure 6a shows results of the repeatability tests of SnO<sub>2</sub> NT sensor. The errors (= standard deviation/mean  $\times$  100 (%)) were 8.9% at 1 ppm, 4.2% at 5 ppm, 1% at 10 ppm, and 0.02% at 20 ppm. Figure 6b shows results of the repeatability test of the SnO<sub>2</sub>–ZnO hybrid nanostructure-based sensor. Likewise, errors were 7.4% at 1 ppm, 7.5% at 5 ppm, 2.6% at 10 ppm, and 0.09% at 20 ppm. Therefore, it is proved that both materials have excellent stability when repeatedly exposed to the gas, and the sensor signal stably appears without irreversible change even after exposure to high concentrations. In addition, an excellent mechanical reliability of the microheater was also confirmed by long-term operation for 1 week, as shown in Figure S5 in the Supporting Information. Here, the electrical resistance of the microheater remained almost constant with a standard deviation of 0.196% at a heating power of 5 mW.

Next, we examined the sensitivity variation between the sensors of the same type. Four different sensors from the same LPD batch were tested twice for each at 5 mW of operating power so that totally 8 tested results were used. The error rate was defined as standard deviation/mean  $\times$  100 (%). Figure 6c,d shows variation of the sensitivity of SnO<sub>2</sub> NTs and SnO<sub>2</sub>–ZnO hybrid nanostructures. In both cases, errors were within 27 and 21%, respectively. These errors may have come from the accumulation of the processing deviation from the fabrication of the microheater to the final LPD process and the random network formed by a number of 1-D nanostructures. It has been reported that the sensitivity–concentration relationship of SMO gas sensors can be fitted to a power function ( $S = 1 + aP_{\text{gas}}^b$ ,  $S$  = sensitivity ( $R_a/R_g$ ),  $P_{\text{gas}}$  = partial pressure of gas,  $a$ ,  $b$  = coefficient).<sup>19</sup> The sensitivity–concentration relationship for the SnO<sub>2</sub> NT and SnO<sub>2</sub>–ZnO hybrid nanostructures was calculated as  $S = 1 + 2602P_{\text{gas}}^{0.491}$  and  $S = 1 + 72\,930P_{\text{gas}}^{0.729}$ , respectively. Previous studies have shown that the coefficient  $b$  for SnO<sub>2</sub> is close to 0.5 for the reducing gas, and the result from this study ( $b = 0.491$ ) is also well matched.<sup>19</sup> With this obtained sensitivity–concentration relationship, when the sensor is exposed to the arbitrary H<sub>2</sub>S gas, the concentration of gas can be estimated by inverse calculation from the sensor signal. It is well known that SMO gas sensors are not highly selective for a particular target gas. Here, the gas selectivity of our sensor was tested with 1 ppm of nitrogen dioxide (NO<sub>2</sub>),

hydrogen sulfide (H<sub>2</sub>S), carbon monoxide (CO), toluene (C<sub>6</sub>H<sub>5</sub>–CH<sub>3</sub>), and ammonia (NH<sub>3</sub>) gases. As shown in Figure S6 in the Supporting Information, hydrogen sulfide showed the greatest sensitivity ( $R_a/R_g = 3.4$ ) among the reducing gases (i.e., hydrogen sulfide (H<sub>2</sub>S), carbon monoxide (CO), toluene (C<sub>6</sub>H<sub>5</sub>–CH<sub>3</sub>), and ammonia (NH<sub>3</sub>)). Nitrogen dioxide (NO<sub>2</sub>), which is an oxidizing gas, showed reverse sensitivity ( $R_a/R_g < 1$ ), indicating the resistance increase. It will be possible to further increase the selectivity by coating the surface of sensing materials with catalysts (e.g., Pd or Pt), which can selectively react with specific gases.<sup>11,29–32</sup>

## CONCLUSIONS

In summary, we have suggested a facile fabrication method to effectively combine MEMS heating platforms and 1-D nanomaterials for high performance SMO gas sensors. This method is based on sequential liquid-phase process consisting of localized hydrothermal synthesis and LPD. By using this sequential process, ZnO NWs could be locally synthesized in microscale area on freestanding MEMS device and then substituted to porous SnO<sub>2</sub> NTs through LPD. By controlling the LPD condition (i.e., pH), the amount of ZnO remaining in the SnO<sub>2</sub> tube could be modulated. As a result, we could synthesize SnO<sub>2</sub>–ZnO hybrid nanostructures as well as SnO<sub>2</sub> NTs. Synthesized SnO<sub>2</sub> NTs showed excellent sensitivity, response speed, and stability to H<sub>2</sub>S gas. Especially, SnO<sub>2</sub>–ZnO hybrid nanostructures showed further enhancement of sensitivity due to a heterojunction effect. By overcoming the limitations of downscaling of conventional nanomaterial integration methods, one of the lowest power SMO gas sensor with excellent performance could be achieved. The proposed method, based on a low-temperature liquid-phase process requiring only a small amount of precursor solution, is environmentally friendly and low in cost compared with the conventional vapor synthesis method. In addition, it will be very useful for the fabrication of various oxide-based electronic devices. In future, a low-power electronic nose system will be realized by integrating a 1-D nanomaterial array (e.g., SnO<sub>2</sub>, CuO, ZnO, and TiO<sub>2</sub>) into a single chip through a sequential liquid-phase process for multiplexed detection of various gas species.

## ASSOCIATED CONTENT

### Supporting Information

The Supporting Information is available free of charge on the ACS Publications website at DOI: 10.1021/acsami.7b04850.

Design of microheaters, temperature–power relationship, mechanism of liquid-phase deposition of SnO<sub>2</sub>, TEM analysis of ZnO nanowires, SnO<sub>2</sub> nanotubes and SnO<sub>2</sub>–ZnO hybrid nanostructure, mechanical reliability of the fabricated microheater, gas selectivity test, gas testing setup, and Figures S1–S7 (PDF)

## AUTHOR INFORMATION

### Corresponding Author

\*E-mail: inkyu@kaist.ac.kr.

### ORCID

Daejong Yang: 0000-0002-8774-5843

Inkyu Park: 0000-0001-5761-7739

## Author Contributions

The article was written through contributions of all authors. All authors have given approval to the final version of the article.

## Notes

The authors declare no competing financial interest.

## ACKNOWLEDGMENTS

This work was supported by Basic Science Research Programs (No. 2015R1A5A1037668) through the National Research Foundation (NRF) funded by the Korean government.

## REFERENCES

- (1) Neri, G. First Fifty Years of Chemosensitive Gas Sensors. *Chemosensors* **2015**, *3*, 1–20.
- (2) Ponzoni, A.; Comini, E.; Sberveglieri, G.; Zhou, J.; Deng, S. Z.; Xu, N. S.; Ding, Y.; Wang, Z. L. Ultrasensitive and Highly Selective Gas Sensors using Three-Dimensional Tungsten Oxide Nanowire Networks. *Appl. Phys. Lett.* **2006**, *88*, No. 203101.
- (3) Li, B.; Santhanam, S.; Schultz, L.; Jeffries-El, M.; Iovu, M. C.; Sauv e, G.; Cooper, J.; Zhang, R.; Revelli, J. C.; Kusne, A. G.; et al. Inkjet Printed Chemical Sensor Array Based on Polythiophene Conductive Polymers. *Sens. Actuators, B* **2007**, *123*, 651–660.
- (4) Mishra, S.; Barton, K. L.; Alleyne, A. G.; Ferreira, P. M.; Rogers, J. A. High-Speed and Drop-on-Demand Printing with a Pulsed Electrohydrodynamic Jet. *J. Micromech. Microeng.* **2010**, *20*, No. 095026.
- (5) Zhou, Q.; Sussman, A.; Chang, J.; Dong, J.; Zettl, A.; Mickelson, W. Fast Response Integrated MEMS Microheaters for Ultra Low Power Gas Detection. *Sens. Actuators, A* **2015**, *223*, 67–75.
- (6) Long, H.; Harley-Trochimczyk, A.; He, T.; Pham, T.; Tang, Z.; Shi, T.; Zettl, A.; Mickelson, W.; Carraro, C.; Maboudian, R. In Situ Localized Growth of Porous Tin Oxide Films on Low Power Microheater Platform for Low Temperature CO Detection. *ACS Sens.* **2016**, *1*, 339–343.
- (7) Xu, L.; Dai, Z.; Duan, G.; Guo, L.; Wang, Y.; Zhou, H.; Liu, Y.; Cai, W.; Wang, Y.; Li, T. Micro/Nano Gas Sensors: A New Strategy Towards In-Situ Wafer-Level Fabrication of High-Performance Gas Sensing Chips. *Sci. Rep.* **2015**, *5*, No. 10507.
- (8) Yang, D.; Kim, D.; Ko, S. H.; Pisano, A. P.; Li, Z.; Park, I. Focused Energy Field Method for the Localized Synthesis and Direct Integration of 1D Nanomaterials on Microelectronic Devices. *Adv. Mater.* **2015**, *27*, 1207–1215.
- (9) Yang, D.; Fuadi, M. K.; Kang, K.; Kim, D.; Li, Z.; Park, I. Multiplexed Gas Sensor Based on Heterogeneous Metal Oxide Nanomaterial Array Enabled by Localized Liquid-Phase Reaction. *ACS Appl. Mater. Interfaces* **2015**, *7*, 10152–10161.
- (10) Yang, D.; Kang, K.; Kim, D.; Li, Z.; Park, I. Fabrication of Heterogeneous Nanomaterial Array by Programmable Heating and Chemical Supply within Microfluidic Platform towards Multiplexed Gas Sensing Application. *Sci. Rep.* **2015**, *5*, No. 8149.
- (11) Kim, D.; Yang, D.; Kang, K.; Lim, M. A.; Li, Z.; Park, C.-O.; Park, I. In-Situ Integration and Surface Modification of Functional Nanomaterials by Localized Hydrothermal Reaction for Integrated and High Performance Chemical Sensors. *Sens. Actuators, B* **2016**, *226*, 579–588.
- (12) Jin, C. Y.; Yun, J.; Kim, J.; Yang, D.; Kim, D. H.; Ahn, J. H.; Lee, K.-C.; Park, I. Highly Integrated Synthesis of Heterogeneous Nanostructures on Nanowire Heater Array. *Nanoscale* **2014**, *6*, 14428–14432.
- (13) Jin, C. Y.; Li, Z.; Williams, R. S.; Lee, K.-C.; Park, I. Localized Temperature and Chemical Reaction Control in Nanoscale Space by Nanowire Array. *Nano Lett.* **2011**, *11*, 4818–4825.
- (14) Choi, K. J.; Jang, H. W. One-Dimensional Oxide Nanostructures as Gas-Sensing Materials: Review and Issues. *Sensors* **2010**, *10*, 4083–4099.
- (15) Greene, L. E.; Law, M.; Tan, D. H.; Montano, M.; Goldberger, J.; Somorjai, G.; Yang, P. General Route to Vertical ZnO Nanowire Arrays using Textured ZnO Seeds. *Nano Lett.* **2005**, *5*, 1231–1236.
- (16) Cai, N.; Cho, J. Low Temperature Processed SnO<sub>2</sub> Films using Aqueous Precursor Solutions. *Ceram. Int.* **2013**, *39*, 143–151.
- (17) Saito, Y.; Sekiguchi, Y.; Mizuhata, M.; Deki, S. Continuous Deposition System of SnO<sub>2</sub> Thin Film by the Liquid Phase Deposition (LPD) Method. *J. Ceram. Soc. Jpn.* **2007**, *115*, 856–860.
- (18) Barsan, N.; Schweizer-Berberich, M.; G opel, W. Fundamental and Practical Aspects in the Design of Nanoscaled SnO<sub>2</sub> Gas Sensors: A Status Report. *Fresenius' J. Anal. Chem.* **1999**, *365*, 287–304.
- (19) Park, C. O.; Akbar, S. Ceramics for Chemical Sensing. *J. Mater. Sci.* **2003**, *38*, 4611–4637.
- (20) Choi, S.-W.; Park, J. Y.; Kim, S. S. Synthesis of SnO<sub>2</sub>-ZnO Core-Shell Nanofibers via a Novel Two-Step Process and Their Gas Sensing Properties. *Nanotechnology* **2009**, *20*, No. 465603.
- (21) Wagh, M.; Patil, L.; Seth, T.; Amalnerkar, D. Surface Cupricated SnO<sub>2</sub>-ZnO Thick Films as a H<sub>2</sub>S Gas Sensor. *Mater. Chem. Phys.* **2004**, *84*, 228–233.
- (22) Kim, K.-W.; Cho, P.-S.; Kim, S.-J.; Lee, J.-H.; Kang, C.-Y.; Kim, J.-S.; Yoon, S.-J. The Selective Detection of C<sub>2</sub>H<sub>5</sub>OH using SnO<sub>2</sub>-ZnO Thin Film Gas Sensors Prepared by Combinatorial Solution Deposition. *Sens. Actuators, B* **2007**, *123*, 318–324.
- (23) Deki, S.; Iizuka, S.; Mizuhata, M.; Kajinami, A. Fabrication of Nano-Structured Materials from Aqueous Solution by Liquid Phase Deposition. *J. Electroanal. Chem.* **2005**, *584*, 38–43.
- (24) Huang, H.; Gong, H.; Chow, C. L.; Guo, J.; White, T. J.; Tse, M. S.; Tan, O. K. Low-Temperature Growth of SnO<sub>2</sub> Nanorod Arrays and Tunable n-p-n Sensing Response of a ZnO/SnO<sub>2</sub> Heterojunction for Exclusive Hydrogen Sensors. *Adv. Funct. Mater.* **2011**, *21*, 2680–2686.
- (25) Yu, J. H.; Choi, G. M. Electrical and CO Gas Sensing Properties of ZnO-SnO<sub>2</sub> Composites. *Sens. Actuators, B* **1998**, *52*, 251–256.
- (26) Park, J.-A.; Moon, J.; Lee, S.-J.; Kim, S. H.; Chu, H. Y.; Zyung, T. SnO<sub>2</sub>-ZnO Hybrid Nanofibers-Based Highly Sensitive Nitrogen Dioxides Sensor. *Sens. Actuators, B* **2010**, *145*, 592–595.
- (27) Khoang, N. D.; Van Duy, N.; Hoa, N. D.; Van Hieu, N.; et al. Design of SnO<sub>2</sub>/ZnO Hierarchical Nanostructures for Enhanced Ethanol Gas-Sensing Performance. *Sens. Actuators, B* **2012**, *174*, 594–601.
- (28) Malyshev, V.; Vasiliev, A.; Eryshkin, A.; Kolytyn, E.; Shubin, Y. I.; Buturlin, A.; Zaikin, V.; Chakhunashvili, G. Gas Sensitivity of SnO<sub>2</sub> and ZnO Thin-Film Resistive Sensors to Hydrocarbons, Carbon Monoxide and Hydrogen. *Sens. Actuators, B* **1992**, *10*, 11–14.
- (29) Yun, J.; Jin, C. Y.; Ahn, J.-H.; Jeon, S.; Park, I. A Self-Heated Silicon Nanowire Array: Selective Surface Modification with Catalytic Nanoparticles by Nanoscale Joule Heating and Its Gas Sensing Applications. *Nanoscale* **2013**, *5*, 6851–6856.
- (30) Choi, B.-S.; Lee, Y. W.; Kang, S. W.; Hong, J. W.; Kim, J.; Park, I.; Han, S. W. Multimetallic Alloy Nanotubes with Nanoporous Framework. *ACS Nano* **2012**, *6*, 5659–5667.
- (31) Lee, Y. W.; Lim, M. A.; Kang, S. W.; Park, I.; Han, S. W. Facile Synthesis of Noble Metal Nanotubes by Using ZnO Nanowires as Sacrificial Scaffolds and Their Electrocatalytic Properties. *Chem. Commun.* **2011**, *47*, 6299–6301.
- (32) Lim, M. A.; Lee, Y. W.; Han, S. W.; Park, I. Novel Fabrication Method of Diverse One-Dimensional Pt/ZnO Hybrid Nanostructures and Its Sensor Application. *Nanotechnology* **2010**, *22*, No. 035601.